Journal of
Marine Science and Engineering

MDPI

Article

Late Holocene Climate Warming Events and Their Linkage to Hydraulic Engineering on the Coast of Hangzhou Bay, East China

Xunpeng Li [1], Xiaolei You [2], Sen Lin [3], Wentong Zhang [1], Zeen Cheng [2] and Zhanghua Wang [1,4,*]

[1] State Key Laboratory of Estuarine and Coastal Research, East China Normal University, Shanghai 200241, China; 51213904012@stu.ecnu.edu.cn (X.L.); 52183904025@stu.ecnu.edu.cn (W.Z.)
[2] Zhejiang Institute of Cultural Relics and Archaeology, Hangzhou 310014, China; xlyouz@163.com (X.Y.); cze09c16@sina.com (Z.C.)
[3] Hangzhou Institute of Cultural Relics and Archaeology, Hangzhou 310002, China; iarchaeologyart@163.com
[4] Southern Marine Science and Engineering Guangdong Laboratory (Zhuhai), Zhuhai 519080, China
* Correspondence: zhwang@geo.ecnu.edu.cn

Abstract: The coastal lowlands in East China are very sensitive to climate change and marine disasters, and much large-scale hydraulic engineering was recorded in the historical documents of the Late Holocene. In this study, AMS ^{14}C and OSL were used to date three sedimentary profiles from the north and south coasts of inner Hangzhou Bay, and grain size and geochemical analyses including organic carbon, macro-elements, and alkaline earth metals were performed, while hydraulic engineering records in historical documents were compiled, in an attempt to reveal the sedimentary records of extreme climatic and hydrological events over the past 3000 years and to probe into the correlation between them and hydraulic engineering. The results show that the intensified chemical weathering during ca. 200 BCE to 900 CE in East China corresponded to the warm and humid climate during the Qin-Han and Sui-Tang dynasties. Salinity intrusion with rising local water levels occurred in the lowland plains along the south coast of Hangzhou Bay from 120 to 895 CE. Low-salinity water intrusion from 32 to 488 CE was also recorded in the stratigraphy of lowland plains along the north coast of Hangzhou Bay. The sedimentary records of the East Tiaoxi River basin show river floods about 2000 years ago. The above sedimentary records indicate that the relative sea level rose in the Hangzhou Bay area during the Qin-Han and Sui-Tang Warm Periods, resulting in frequent salinity intrusion and river floods, which coincided with the historical records of hydraulic engineering such as the construction of seawalls, river levees, and the enclosure of lakes for restoration of river floods during the Han and Tang dynasties. Such coincidence reflects that climate change profoundly affected the hydrological environment of the coastal areas in East China as well as the response of the human societies.

Keywords: salinity intrusion; river flood; relative sea-level rise; chemical weathering; Qin-Han warm period; Sui-Tang warm period

check for updates

Citation: Li, X.; You, X.; Lin, S.; Zhang, W.; Cheng, Z.; Wang, Z. Late Holocene Climate Warming Events and Their Linkage to Hydraulic Engineering on the Coast of Hangzhou Bay, East China. *J. Mar. Sci. Eng.* **2024**, *12*, 79. https://doi.org/10.3390/jmse12010079

Academic Editor: Assimina Antonarakou

Received: 6 December 2023
Revised: 25 December 2023
Accepted: 25 December 2023
Published: 29 December 2023

1. Introduction

Rapid development of human societies in the late Holocene significantly increased the human–environment interactions [1–4]. Previous researchers have reconstructed the paleoclimate from high-resolution archives such as ice cores [5], speleothems [6], tree rings [7], and lake sediments [8], as well as phenological information from historical documentary sources [9,10]. These studies have revealed a series of centennial-decadal climate fluctuations in the late Holocene, such as the "2.8 ka" event, the Roman Warm Period, the Dark Ages Cold Period, the Sui-Tang Warm Period, the Medieval Climate Anomaly, and the Little Ice Age [11–16], and these climate events have made significant impacts on human societies [17,18]. During the Late Holocene, with the growing population and economic and technological advancements, humans responded to climate change more by modifying the natural environment. Hydraulic engineering was usually constructed to address the requirements of flood control, storm defense, as well as irrigation and water storage, especially for the agricultural societies [19–22]. Therefore, an objective assessment of major climate events during the Late Holocene and the response and adaptation strategies employed by human societies can offer valuable insights for addressing the current climate crisis.

The coastal plain of Hangzhou Bay in East China (Figure 1) had served as a significant population center since the Neolithic period and was the location of the Liangzhu hydraulic engineering system constructed approximately 5000 years ago, which is the earliest large-scale hydraulic project in East Asia (Figure 1b) [23]. During the historical period, a number of hydraulic engineering occurred here (Figure 1c), not only the construction of seawalls to defense storm tides in Hangzhou Bay but also the construction of large reservoirs/artificial lakes and river levees in the hinterland, which were used to control river floods [24–26]. Some researchers have suggested that the current East Tiaoxi River washing against the northwest wall of Liangzhu City (Figure 1b) was redirected following the construction of the Great Xixian Levee in 173 CE during the Eastern Han Dynasty [27]. Therefore, the coast along Hangzhou Bay is an ideal place to study major climatic events and the human response of hydraulic engineering during the historical period.

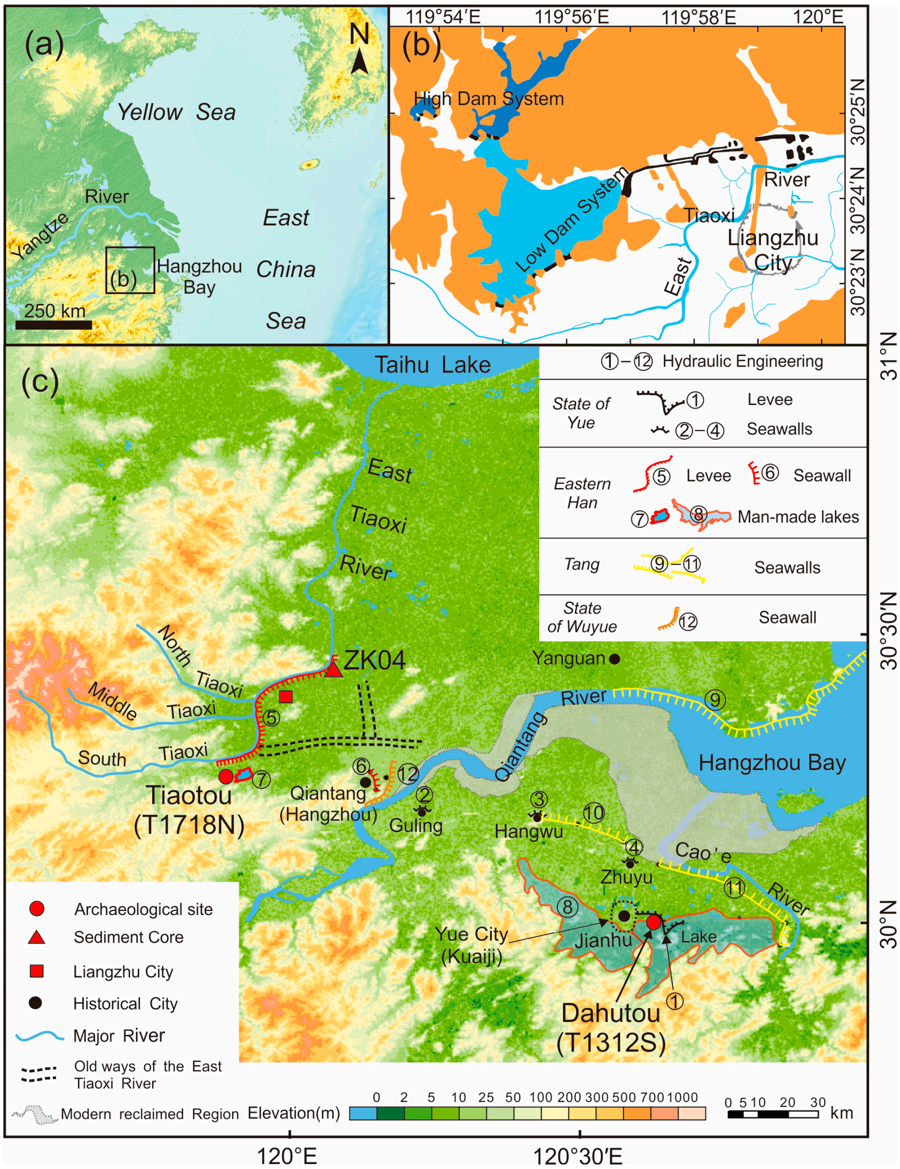

Figure 1. Geographic locations of Hangzhou Bay and sediment profiles and core used in the present study: (**a**) The geographical position of Hangzhou Bay in East Asia; (**b**) Liangzhu hydraulic engineering

and East Tiaoxi River which currently washes against the northwestern wall of Liangzhu City [28]; (**c**) The topography and water system of the study area, locations of the sediment profiles, core, and the important hydraulic engineering in the historical period. Markers ① to ④ are the hydraulic engineering of the Yue State: ① The Great Fuzhong Seawall; ② to ④ Seawalls. ⑤ to ⑧ and the enclosed area are the hydraulic engineering projects of the Eastern Han Dynasty: ⑤ Great Xixian Levee; ⑥ Seawall; ⑦ South Lake; ⑧ Jianhu Lake; ⑨ to ⑪ are the seawalls of the Tang Dynasty: ⑨ Yanguan Seawall; ⑩ Shanyin Seawall; ⑪ Kuaiji Seawall; ⑫ is Wuyue seawall.

This study employed sediment profiles from two archaeological sites located in the coastal lowlands of inner Hangzhou Bay and the East Tiaoxi River basin, along with a core acquired at the point where East Tiaoxi River flows northward to the Taihu Lake (Figure 1c). A multi-proxy study including chronology, sedimentology, and elemental geochemistry was carried out for these sedimentary records to reveal the changes in climate and hydrological environment and to identify flood disasters. Together with compiled data from historical documents, this study aims to shed light on the underlying climatic drivers for human's construction of hydraulic engineering along the coast of inner Hangzhou Bay.

2. Geographic Setting of the Study Area

Hangzhou Bay, situated on the coast of East China, is a large funnel-shaped bay (Figure 1a). It is bounded on the north by the Yangtze River mouth and the southern plains of the Yangtze River Delta, on the west and south by mountains, and opens on the east to the East China Sea. The main water systems entering into Hangzhou Bay are the Qiantang River and the Cao'e River (Figure 1c). The mean annual runoff of the Qiantang River is 291×10^8 m^3 and the mean annual sediment load is roughly 500×10^4 tons [29]. The mean annual runoff of the Cao'e River is 31.05×10^8 m^3, and the mean annual sediment load is roughly 66.37×10^4 tons [30]. The East Tiaoxi River is the major water system discharging into the Taihu Lake on the north bank of Hangzhou Bay. It originates from multiple mountain streams in the area atop Hangzhou Bay, converges in the west side of Liangzhu City, flows eastward, and ultimately turns north before entering Taihu Lake (Figure 1c).

After the tidal wave from the East China Sea enters Hangzhou Bay, it generates a clockwise rotating tide with a flow velocity of approximately 1.5–2.0 m/s [29]. Due to the funnel-like shape of Hangzhou Bay, the tides become amplified as the tidal range increases and tidal currents strengthen. The development of sand shoal at the mouth of the Qiantang River further deforms and breaks up the tidal wave, resulting in the formation of a remarkable surge. The average tidal range in the top area of Hangzhou Bay is approximately 5.45 m [31,32].

Hangzhou Bay experiences frequent typhoon activities during the summer and autumn seasons. Instrumental data from 1951 to 2005 indicate that around 1.6 typhoons impact the area every year, with typhoon storm surges being the major natural disaster in the region, which is particularly intensified by the geometry and subaqueous topography of the bay [33,34]. For instance, Typhoon "Canhong" in July 2015 caused water levels to rise in Hangzhou Bay with a maximum value of 1.2–3.0 m from the mouth to the top [35].

3. Materials and Methods

The sites of Dahutou in Shaoxing (29°59′40.74″ N, 120°37′45.73″ E) and Tiaotou in Yuhang (30°15′00″ N, 119°53′39″ E) are situated in the coastal plain on the southern bank of inner Hangzhou Bay and the middle reaches of East Tiaoxi River on the northern coast, respectively. The Dahutou site is situated on the southern side of the Great Fuzhong Seawall, an example of substantial hydraulic engineering constructed in the Warring States Period, i.e., the State of Yue during the Eastern Zhou dynasty (Figures 1c and 2). This site was excavated in 2022 and is characterized by the accumulation of Yue cultural layers. Profile T1312S was collected from the site's edge at a 4.757 m ground elevation and with a depth of 113 cm. The Tiaotou site is on the southwest coast of South Lake, which was an artificial lake constructed during the Eastern Han Dynasty and reclaimed largely several decades ago. Located in the alluvial piedmont plain of the East Tiaoxi River basin, the ground elevation at the site is approximately 8 m. Archaeological excavations in 2021 have shown that the Tiaotou site was a copper-casting workshop site during the Late Shang period. A buried river channel, 30 m wide, was also uncovered in the excavation area. A previous study reported that this channel served as a water storage area for the copper-casting activities in the Late Shang period, but eventually became a natural river channel during later times; lastly, the river channel submerged into the South Lake after the lake was enclosed [36]. In this study, a sedimentary profile T1718 N with a depth of 175 cm was obtained on the east bank of the channel where it was the edge of residential area during the Late Shang Dynasty. Additionally, sediment core ZK04 (30°26′17.85″ N, 120°04′20.13″ E) was obtained with a depth of 20 m in 2019 from a location where the East Tiaoxi River turns northward in the Taihu Lake plain (Figure 1c). This location is about 1 km from the current river channel and has a ground elevation of 3.870 m. The upper 12 m of the sediment core was chosen for examination based on lithological observation.

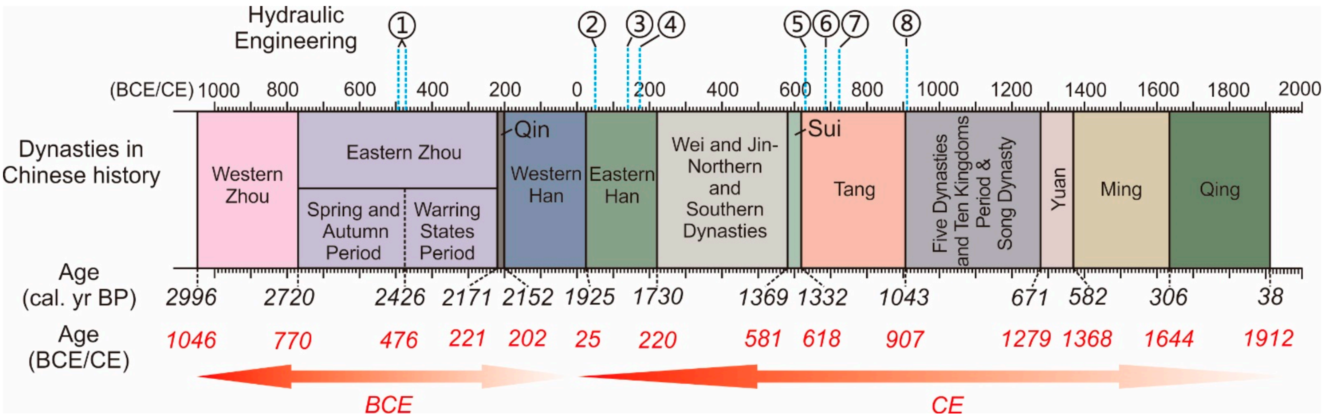

Figure 2. Timeline of dynasties in Chinese history. The Yue State was one of the Warring States during the late period of Eastern Zhou and the Wuyue State belongs to the period of the Five Dynasties and Ten Kingdoms. Also indicated are the major hydraulic engineering events (①–⑧) that took place on the coast of Hangzhou Bay recorded in historical documents: ① The hydraulic engineering of Yue State (493–473 BCE); ② The seawall of Eastern Han (50 CE); ③ Jianhu Lake (140 CE); ④ Great Xixian Levee and South Lake (173 CE); ⑤ Yanguan Seawall (630 CE); ⑥ Shanyin Seawall (686 CE); ⑦ Kuaiji Seawall (722 CE); ⑧ Wuyue Seawall (910 CE).

We collected profiles T1312S and T1718N using U-troughs during the archaeological excavation in the Dahutou and Tiaotou sites, while sediment core ZK04 was drilled using a mechanical rig with a core diameter of 88 mm enclosed in PVC piping. Before sampling, fresh surfaces of the two profiles were cut in the excavation units for lithostratigraphic observations, including color, texture and structure, macro-bio remains, and contacts between strata. Charcoals and plant remains were selected from the fresh surfaces for radiocarbon dating. U-trough samples were transported to the laboratory where they were sliced into 2 cm intervals. The sediment core was cut in the laboratory to observe the lithology and collect dating samples, which was further divided into 2 cm intervals.

Three samples of charcoal and one sample of plant debris were selected from profile T1312S at the Dahutou site. Four samples of charcoal were collected from profile T1718N at the Tiaotou site. Additionally, one sample of plant debris was obtained from sediment core ZK04. After completing preliminary pretreatment at the State Key Laboratory of Estuarine and Coastal Research of East China Normal University, the samples were sent to Beta Company for AMS ^{14}C dating. The obtained ^{14}C ages were calibrated using the IntCal 20 curve of the Calib 8.2 program (Table 1) [37]. Two sediment samples were chosen from core ZK04 and dated through Optically Stimulated Luminescence (OSL) using the quartz grains of 45–63 µm at the State Key Laboratory of Estuarine and Coastal Research, East China

Normal University. The U, Th, and K contents were analyzed using the neutron activation method (NAA) at the China Institute of Atomic Energy in Beijing. Environmental dose rates and chronology results were calculated and corrected using "LDVC (v 1.2)" software [38], and OSL ages were calculated using a minimum age model (Table 2) [39]. All OSL ages have also been corrected to calendar ages to be consistent with the calibrated ^{14}C ages.

Table 1. ^{14}C dating results and calibrated ages of profiles T1312S and T1718N and core ZK04.

Profile/Core	Depth (cm)	Material	$\delta^{13}C$ (‰)	Conventional Age (yr BP)	Calibrated Age (cal. yr BP)			Median (BCE/CE)	Laboratory Number
					2 Sigma	Prob.	Median		
T1312S	43	Charcoal	−23.9	110 ± 30	11–267	1	110	1840 CE	Beta-661596
T1312S	62	Charcoal	−26.8	1370 ± 30	1266–1316	0.824	1295	655 CE	Beta-661597
T1312S	77	Plant	−27.0	2260 ± 30	2155–2343	1	2230	280 BCE	Beta-661598
T1312S	97	Charcoal	−27.6	2290 ± 30	2176–2353	1	2320	370 BCE	Beta-661599
T1718N	34	Charcoal	−25.9	820 ± 30	677–752	0.892	715	1235 CE	Beta-651145
T1718N	67	Charcoal	−26.5	2920 ± 30	2989–3163	0.934	3065	1115 BCE	Beta-651146
T1718N	74	Charcoal	−26.3	2820 ± 30	2848–3004	0.989	2920	970 BCE	Beta-667598
T1718N	131	Charcoal	−25.8	3310 ± 30	3453–3584	0.984	3525	1575 BCE	Beta-667599
ZK04	513	Plant	−27.7	2040 ± 30	1923–2068	0.881	1995	45 BCE	Beta-526272

Table 2. OSL ages of core ZK04. The OSL ages were adjusted to calibrated calendar ages to be consistent with the radiocarbon ages.

Depth (m)	U (ppm)	Th (ppm)	K (%)	Moisture Content (%)	Dose Rate (Gy/ka)	Equivalent Dose [(1)] (Gy)	Age (ka)	Age (cal. yr BP)	Age (BCE/CE)	Laboratory Number
10.42	2.46 ± 0.12	14.80 ± 0.74	1.47 ± 0.07	23.8	2.73 ± 0.09	6.45	2.36 ± 0.08	2290	340 BCE	L714
11.20	1.66 ± 0.08	8.61 ± 0.43	1.57 ± 0.08	20.4	2.31 ± 0.07	18.30 ± 1.46	7.92 ± 0.68	7850	5900 BCE	L715

Note: [(1)] Equivalent dose was measured using small slices (2 mm) and the single-aliquot regenerative-dose (SAR) protocol [40] and was calculated using the minimum age model.

In this study, 37 samples from profile T1312S were analyzed for organic geochemistry, testing for Total Carbon (TC), Total Organic Carbon (TOC), Total Nitrogen (TN), and organic carbon stable isotopes ($\delta^{13}C$). The pretreatment process was performed according to [41]. The TC, TN, and TOC contents were analyzed using the Vario EL III elemental analyzer (Elementar, Langenselbold, Germany) and calibrated using the national standardized aquatic sediments (GSD-9). The relative error was less than 3%. The $\delta^{13}C$ was tested using a Delta plus *XP* Stable Isotope Mass Spectrometer (Thermo Finnigan, USA) using the following reference materials: Caffeine (IAEA-600) (−27.77‰), Cellulose (IAEA-CH-3) (−24.72‰), and Black Carbon (GBW04407, GBW04408) (−22.43‰, −36.91‰), with an error of 0.1‰ in units corresponding to the VPDB standard. The C/N ratio was obtained by calculating the mass of TOC and TN.

Thirty-seven (37) samples from profile T1312S and 34 samples from core ZK04 were analyzed for alkaline earth metals in the acetic acid (HAc)-extracted phase, which can be very sensitive to salinity variations in the sedimentary environments of the land-sea transition zone [42]. The pretreatment procedure was in accordance with [42,43]. The iCAP 7400 Inductively Coupled Plasma Optical Emission Spectrometer (ICP-OES; Thermo Fisher, Waltham, MA, USA) was used to measure the contents of Sr, Ba, and Ca. The quality control samples used were national standardized aquatic sediments (GSD-9), and the recovery of the standardized samples was (100 ± 10)%, with the precision within 5%.

Grain size analysis was performed for 20 samples from profile T1718N and 49 samples from core ZK04. After preparing the sample through pretreatment processes that removed organic matter and carbonates and achieved adequate dispersion, grain size was measured using the LS13320 laser analyzer (Beckman Coulter, Brea, CA, USA).

Twenty (20) samples from profile T1718N were tested for macro-elements Na, K, Al, and Ca. Bulk samples were treated due to the dominance of the fine-grained sediments with weak vertical variation in this profile. The samples were first dried at low temperature and fully ground until they all passed through a 200-mesh sieve. After fully mixing, 0.25 g sediments were placed in a Teflon digestion tube, adding 10 mL of concentrated nitric acid (HNO_3), followed by 3 mL of hydrofluoric acid (HF). Next, the sample was heated on a heating plate (100 °C) for 20 min and then were put into a microwave ablator (Multiwave PRO) to be ablated for 2.5 h. The tube was then taken out, 5 mL of perchloric acid ($HClO_4$) was added, and it was heated to a nearly dry state on a hot plate (180 °C) for about 8 h. After cooling, the samples were diluted with dilute HNO_3 (0.1%) in 50 mL volumetric flasks and shaken well to prepare for testing. The iCAP 7400 Inductively Coupled Plasma Optical Emission Spectrometer (ICP-OES; Thermo Fisher, USA) was used to analyze the contents of the above elements (ppm). The quality control sample was national standardized aquatic sediment (GSD-9), with a recovery rate of the standardized sample of (100 ± 10)%, and the precision of the test was within 5%. We further calculated three chemical weathering indices, CIA, CIW, and PIA using the formulas below.

CIA (Chemical Index of Alteration) = $[Al_2O_3/(Al_2O_3 + CaO^* + Na_2O + K_2O)] \times 100$, which mainly reflects the degree of mineral weathering in the source area [44,45].

CIW (Chemical Index of Weathering) = $[Al_2O_3/(Al_2O_3 + CaO^* + Na_2O)] \times 100$ [46], which avoids the potassium metasomatism during the formation of clay minerals [47].

PIA (Plagioclase Index of Alteration) = $[(Al_2O_3 - K_2O)/(Al_2O_3 + CaO^* + Na_2O - K_2O)] \times 100$, an index indicating the degree of plagioclase weathering [47].

The oxides in above expressions are all molar contents, and CaO* is the molar content of CaO in silicate minerals [48,49]. Because this study tested the elemental contents in the bulk sample, which included CaO in carbonate minerals, a correction was implemented using McLennan's method [48]. According to this method, the ratio of CaO to Na_2O in silicate minerals is 1:1. Thus, if the ratio exceeded 1, the Na_2O content was used to substitute CaO in the calculation. Additionally, the ratio of Na_2O/K_2O was calculated, which serves as an indicator of the plagioclase weathering. This ratio exhibits a negative correlation with chemical weathering degrees, as plagioclase is more prone to weathering when compared to the potassium feldspars, with Na being lost more readily than K [50].

All sample pre-treatment and grain size and geochemical analyses were conducted at the State Key Laboratory of Estuarine and Coastal Research, East China Normal University.

In addition, hydraulic engineering along Hangzhou Bay reported by previous studies based on historical documents [24–27,51,52] were collated (Figure 2) for comparing with the hydrological and climatic environments recorded in the stratigraphy.

4. Results

4.1. Major Hydraulic Engineering along the Coast of Inner Hangzhou Bay in Historical Periods

Hydraulic engineering along the coast of inner Hangzhou Bay was dominated by seawalls in the historical period (Figure 2). The earliest can be traced back to the State of Yue (770–222 BCE) during the Warring States Period, where stone walls were built in coastal areas such as Zhuyu (a salt production center), Hangwu, and Guling (a naval garrison) (Figure 1c). The people of Yue also constructed a levee near the "Kuaiji" (Yue City) known as "the Great Fuzhong Seawall" to establish grain production bases (Figure 1c). During the Eastern Han Dynasty, Qiantang County (present-day Hangzhou) residents were repeatedly attacked by the tides of Hangzhou Bay. To counter the seawater intrusion, a defense seawall was constructed in 50 CE, which had a history of almost 2000 years [51]. During the Tang Dynasty, coastal flooding and salinity intrusions persisted, leading to the construction of Shanyin Seawall in 686 CE and the Kuaiji Seawall in 722 CE on the south coast of Hangzhou Bay [24,25]. Subsequently, there were two more expansions to the Kuaiji Seawall. Around the middle to late Tang Dynasty, the seawalls on the south coast of Hangzhou Bay were already linked together, forming a relatively complete tide-defense system [52]. On the north coast of Hangzhou Bay, the Yanguan Seawall was built in 630 CE and reinforced in 713 CE, forming a seawall of about 112 km long. During the State of Wuyue, in the year of 910 CE, Qianliu organized the construction of a defense seawall in Hangzhou with a length of about 12 km to safeguard against tidal surges [51]. After the State of Wuyue, repairing and reinforcing the existing system of seawalls dominated [51].

In addition, during the Eastern Han Dynasty, hydraulic engineering to manage river floods also appeared on both coasts of Hangzhou Bay. In 140 CE, Jianhu Lake was enclosed (Figure 1c) with large gates and weirs on the south bank, which is the oldest large-scale, comprehensive, hydraulically engineered structure for water storage and navigation south of the Yangtze River in China [25]. In 173 CE, the Great Xixian Levee was constructed along the south Tiaoxi River to defense river flooding and the South Lake was enclosed to store the flood water [26,27].

4.2. Stratigraphic and Geochemical Changes in Profile T1312S at the Dahutou Site

Profile T1312S was divided into six layers based on the lithology from the bottom upward (Figure 3a). Layer 6 (113–97 cm) was composed of yellowish grey mud with some Fe oxides, weak leaching structure, and a few root traces. The charcoal at 97 cm was dated to 370 BCE. Layer 5 (97–87 cm) was composed of yellowish grey silty mud—the cultural layer of Yue formed during the Warring States Period. Layer 4 (87–71 cm) was also dominated by the cultural layer of Yue and was composed of grey mud with Fe oxides and charcoal. Silt content was higher at the bottom. The plant debris at 77 cm produced an age of 280 BCE, being consistent with the archaeological judgement. Layer 3 (71–59 cm) was composed of dark grey organic-rich mud with peat at the top 5 cm and mud strips at 64 cm. Charcoal at 62 cm was dated to 655 CE. Layer 2 (59–39 cm) was composed of grey silty mud with oxidized root traces and charcoal in the upper part. The charcoal at 43 cm yielded an age of 1840 CE. Layer 1 (39–0 cm) was the modern topsoil and was not sampled. The four dating results present an ideal sequence from the bottom up, and all were used in the Clam program to calculate the age–depth model (Figure 4a) [53].

Organic geochemistry and alkaline earth metal measurements showed a basically synchronized trend, which can be divided into four stages (Figure 5). Stage I (layer 6; before 370 BCE) had low and stable contents of TN, TC, and TOC, with mean values of 0.06%, 0.27%, and 0.18%, respectively; the C/N ratio was stable at about 3.24. The mean value of $\delta^{13}C$ was approximately −24.21‰. The mean contents of Sr, Ca, and Ba are all relatively low at 8.87 mg/kg, 1.64 g/kg, and 22.34 mg/kg, respectively. Additionally, the Sr/Ba ratio showed a decreasing trend upward with a mean value of 0.40.

During stage II (layer 5–4; 370 BCE to 120 CE), TN, TC, TOC, and C/N all increased markedly at the bottom, then remained stable, and subsequently increased again towards the top, with ranges of 0.06–0.49%, 0.30–6.28%, 0.22–6.04%, and 3.90–12.28. $\delta^{13}C$ values (−26.96 to −23.71‰) decreased from the bottom to the top. The contents of Sr, Ca, and Ba remained low, and Ba decreased slightly in the middle. The mean values were 9.09 mg/kg, 1.64 g/kg, and 21.35 mg/kg, respectively. The Sr/Ba ratio was opposite to that of elemental Ba, higher in the middle and lower parts and decreasing upward.

Stage III (layer 3; 120–895 CE), TN, TC, TOC, and C/N all increased rapidly and fluctuated remarkably, with ranges of 0.33–1.49%, 4.99–29.03%, 4.74–28.34%, and 12.28–20.10. The $\delta^{13}C$ showed the lowest values in the whole profile, with a mean of −27.58‰. The Sr and Ca contents also increased rapidly but with significant fluctuations and peaked at the top, with a range of 9.60–28.78 mg/kg and 1.93–6.14 g/kg, respectively. The Ba content increased gradually from bottom to top (33.61–61.16 mg/kg). The change in the Sr/Ba ratio was similar to that of Sr and Ca, with a range of 0.25–0.64.

In stage IV (layer 2; after 895 CE), TN, TC, TOC, and the C/N ratio all decreased obviously and fluctuated very little, with mean values of 0.10%, 1.02%, 0.91%, and 9.47, respectively. $\delta^{13}C$ values increased again, with a mean of −26.12‰. Sr and Ca contents also declined remarkably, with mean values of 9.99 mg/kg and 1.80 g/kg, respectively. The content of Ba was the highest in the whole profile, with a distribution range of 47.79–74.80 mg/kg. Sr/Ba decreased to a mean value of 0.17.

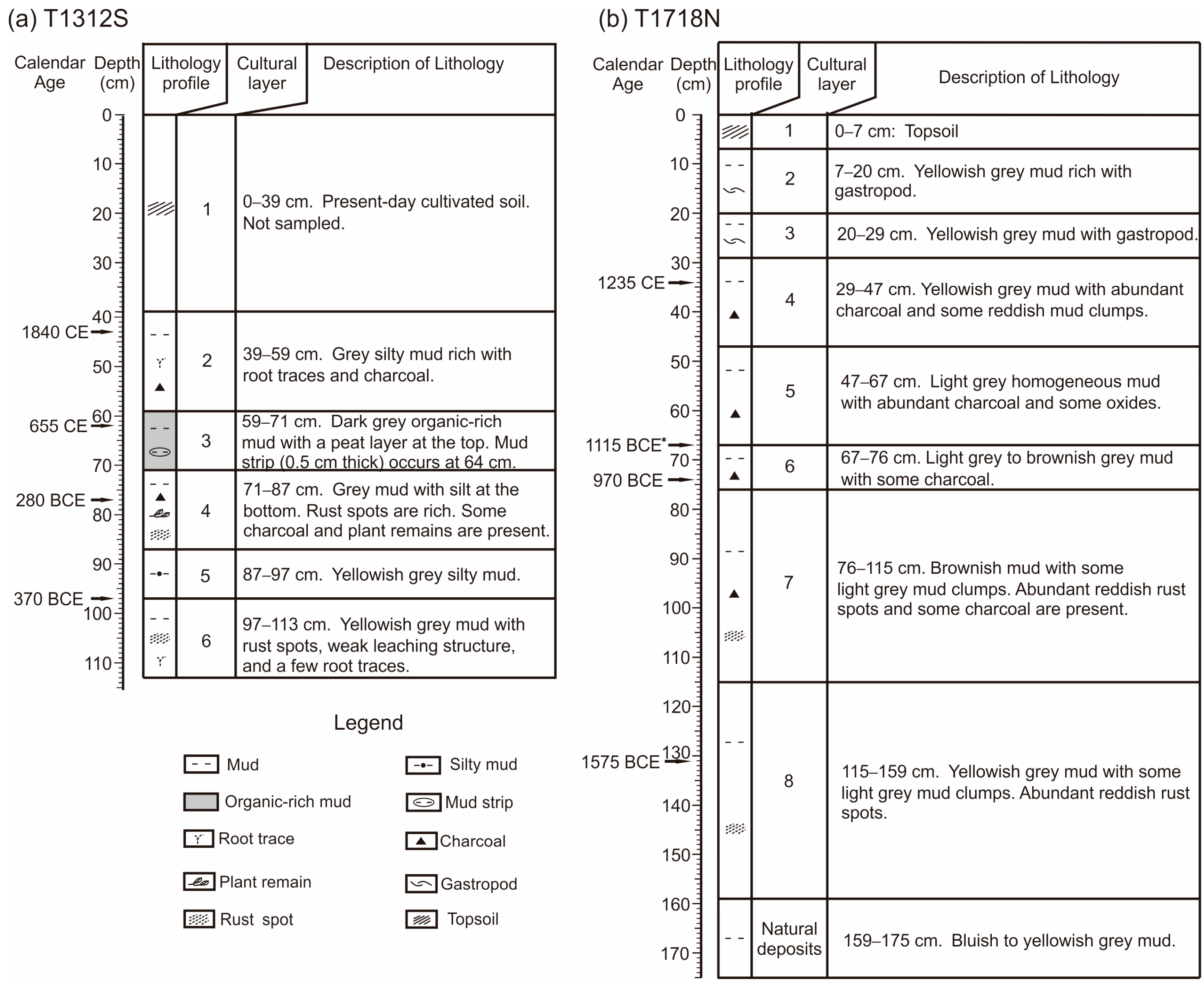

Figure 3. Ages, archeological layers, and lithological descriptions of profiles T1312S (**a**) and T1718N (**b**).

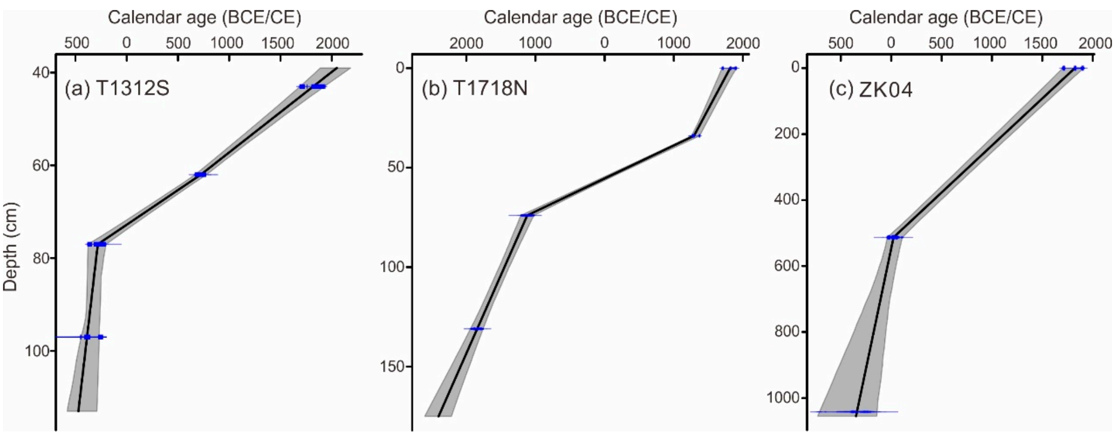

Figure 4. Age-depth model calculated using Clam [53]: (**a**) Profile T1312S; (**b**) Profile T1718N; (**c**) Core ZK04.

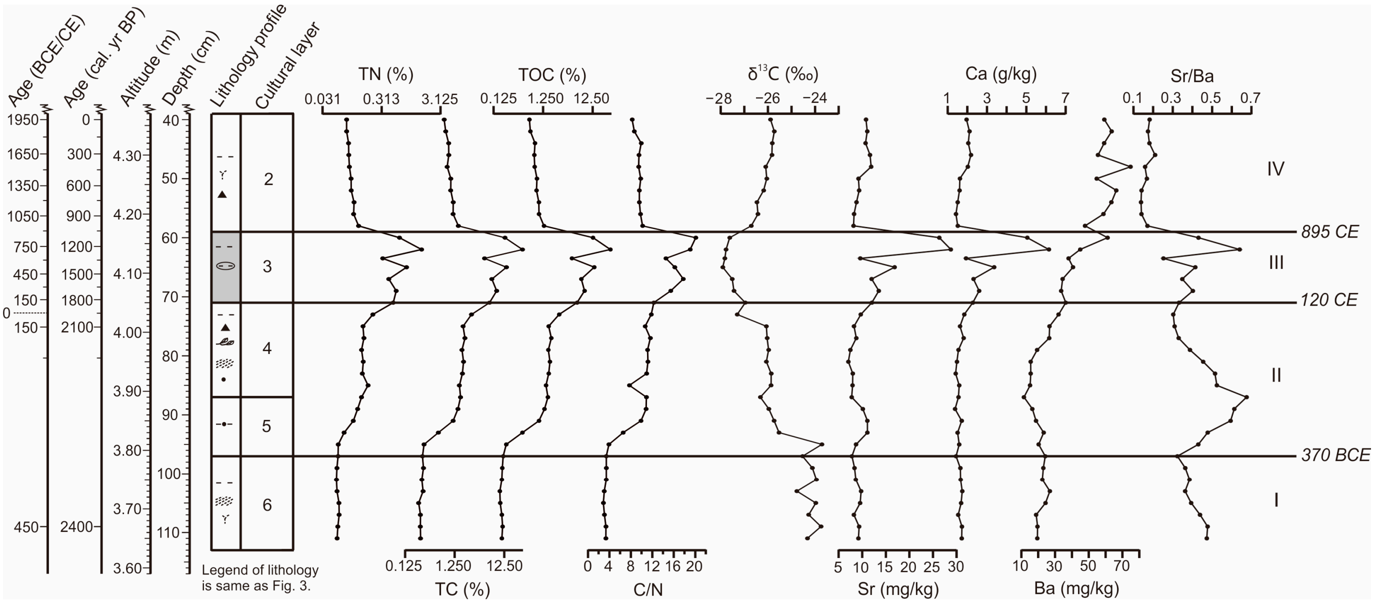

Figure 5. Changes in stratigraphy, organic geochemistry, and alkaline earth metals for profile T1312S. Age coordinate axes calculated according to the Clam age–depth model are also indicated.

4.3. Stratigraphic and Geochemical Changes in Profile T1718N at the Tiaotou Site

Profile T1718N was divided into nine layers from bottom upward according to the lithology (Figure 3b). Layer 9 (175–159 cm) was composed of bluish mud changing upward to yellowish grey mud. Layer 8 (159–115 cm) was composed of yellowish grey mud with a small number of light grey mud clumps, had a large number of reddish rust spots, and was speculated to be the deposits of Shang Dynasty. The charcoal at 131 cm yielded an age of 1575 BCE, consistent with the archaeological judgement. Layer 7 (115–76 cm) was composed of brownish mud with a small number of light grey mud clumps. A large number of reddish rust spots and some charcoal were also found. This layer was suggested to have been formed during the late period of the Shang dynasty. Layer 6 (76–67 cm) was composed of light grey to brownish mud with a small amount of charcoal. The dating result of charcoal at 74 cm was 970 BCE; and the dating result of charcoal at 67 cm was 1115 BCE, being overestimated according to the archaeological judgement. Layer 5 (67–47 cm) was composed of light grey homogeneous mud with a lot of charcoal and a few brownish rust spots. Layer 4 (47–29 cm) was composed of yellowish grey mud with a large amount of charcoal and occasional brick-red clasts. The charcoal at 34 cm was dated to 1235 CE. Layer 3 (29–20 cm) was composed of yellowish grey mud with a few gastropod shells. Layer 2 (20–7 cm) was composed of yellowish grey mud with more gastropod shells. Layer 1 (7–0 cm) was topsoil. After excluding the overestimated age at 67 cm, the other three ages were used in the Clam program to calculate the age–depth model (Figure 4b) [53].

Grain size analysis showed the weak vertical variation in profile T1718N (Figure 6), which is only slightly coarser in layer 8. The mean proportions of clay (0–4 μm), silt (4–63 μm), and sand (>63 μm) in the whole profile were 35.67%, 60.73%, and 3.61%, respectively. The average of the mean grain size was 13.59 μm.

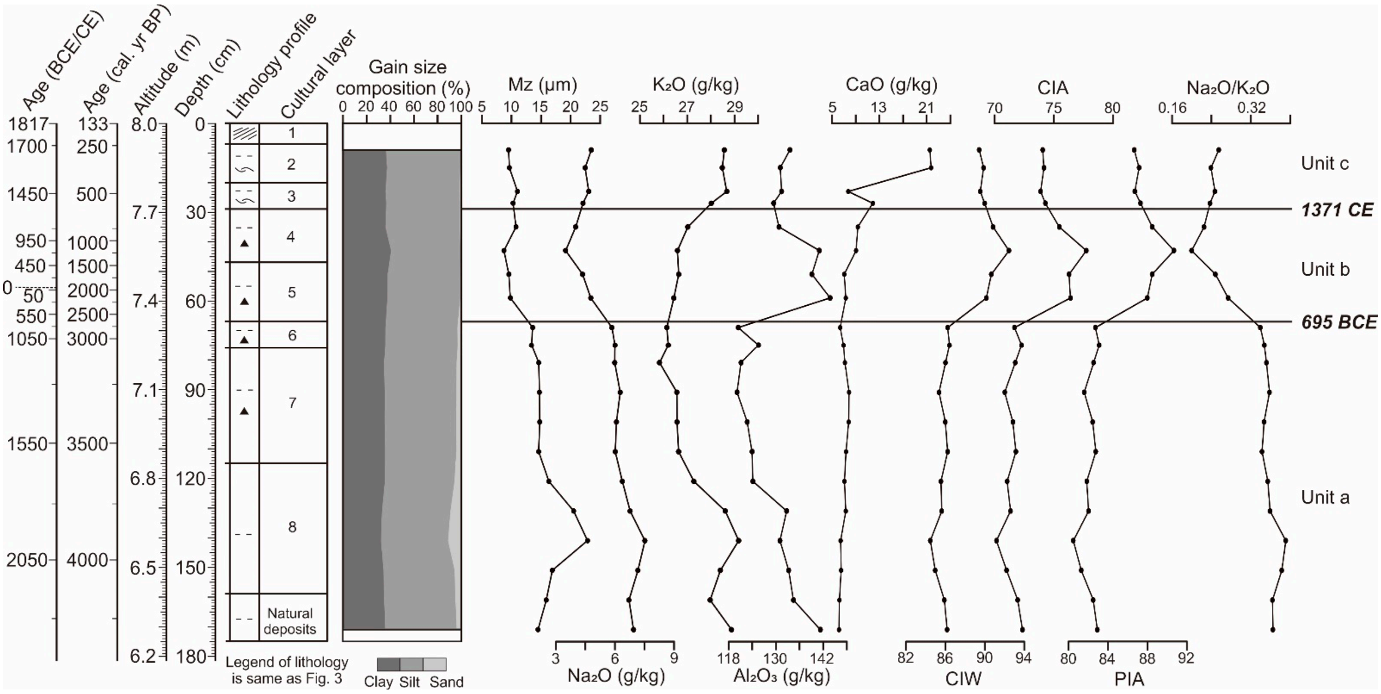

Figure 6. Stratigraphy, grain size composition, elemental content, and chemical weathering index of profile T1718N. Age coordinate axes calculated according to the Clam age–depth model are also indicated.

The vertical variation in the content of each element and chemical weathering index was obvious in profile T1718N (Figure 6). According to their variations, three units were divided from the bottom up: unit a (layer 9–6; before 695 BCE)—Na_2O, K_2O, and Al_2O_3 contents were higher in the lower part and decreased obviously in the upper part, with variations ranging within 5.85–7.52 g/kg, 25.83–29.17 g/kg, and 120.13–141.26 g/kg, respectively. CaO varies insignificantly. CIA, CIW, and PIA were all low, and Na_2O/K_2O was the highest in the whole profile. Unit b (layer 5–4; 695 BCE to 1371 CE), the content of Na_2O (mean value 4.16 g/kg) decreased remarkably, the content of Al_2O_3 (mean value 138.65 g/kg) increased obviously, and the content of K_2O (mean value 26.67 g/kg) and CaO (mean value 8.19 g/kg) increased slightly. CIW, CIA, and PIA remarkably increased as the highest in the whole profile, ranging within 90.15–92.45, 75.46–77.74, and 87.99–90.69, respectively, and Na_2O/K_2O decreased obviously, ranging from 0.20 to 0.27. Those together indicate enhanced chemical weathering. Unit c (layer 3–1; after 1371 CE), the mean value of Na_2O increased slightly to 4.58 g/kg, the mean value of K_2O increased to 28.43 g/kg, and the mean value of Al_2O_3 (mean value 131.37 g/kg) decreased obviously. The CaO was lower in the lower part of the unit and increased dramatically in the upper part of the unit, which was consistent with the fact that more gastropod shells were seen in the upper part, indicating the contribution from the carbonate phase. CIA, CIW, and PIA all declined, with mean values of 74.09, 89.71, and 86.96, respectively, and Na_2O/K_2O rose slightly to 0.24.

4.4. Stratigraphy and Alkaline Earth Metal Variations in Core ZK04

Lithological layering and dating results for core ZK04 are shown below (Figure 7). The depth of 12.00–10.55 m was composed of bluish grey silty sand with occasional laminations of mica. OSL dating gave an age of 5900 BCE at 11.20 m. The depth of 10.55–3.90 m was composed of dark grey silty mud with thin layers of silt below 10 m and a few silt laminations above 7.30 m. Abundant yellowish mud intraclasts were seen at 5.77–5.22 m. The OSL age at 10.42 m was 340 BCE, and the radiocarbon age of plant debris at 5.13 m was 45 BCE. The depth of 3.90–2.27 m was composed of light grey homogeneous mud with a few silt laminations and occasionally some organic-rich bands. The depth of 2.27–1 m was composed of brownish yellow silty mud with abundant yellowish brown rusty spots and Fe/Mn oxides. The depth of 1–0 m was composed of yellowish grey silty mud. According to the fact that the OSL age at 10.42 m was several thousand years younger than the OSL age at 11.2, a depositional hiatus was presumed to have existed at 10.55 m. Thus, the age–depth model using the Clam program [53] was only applied for sediments above 10.55 m using the OSL age at 10.42 m and the radiocarbon age at 5.13 m (Figure 3c).

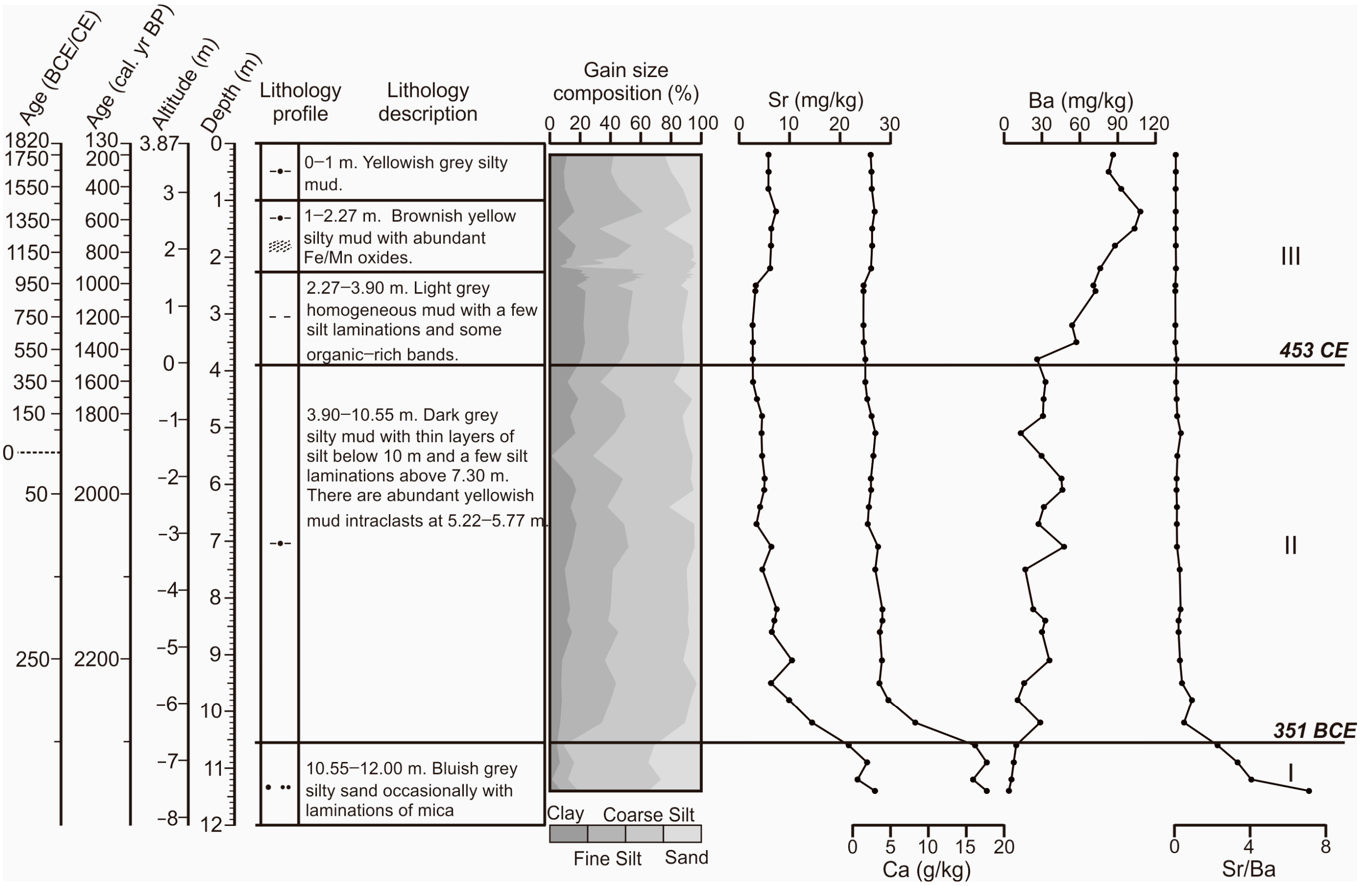

Figure 7. Lithological description, grain size composition, and alkaline earth metals in sediment core ZK04. Age coordinate axes calculated according to the Clam age–depth model are also indicated.

The grain size analysis showed that the content of coarse silt (54.04%) and sand (32.03%) was higher at 12.00–10.55 m, while clay and fine silt were only 4.93% and 9.00%, respectively. Above 10.55 m, the content of sand decreased rapidly and ranged from 3.22% to 24.62%, whereas the average content of clay and fine silt increased to 14.99% and 29.66%, while the content of coarse silt varied little, with a mean value of 46.01%.

Three sections (I–III) were recognized according to the vertical variation in the alkaline earth metals: from 12 to 10.55 m (section I, about 5900 BCE), Sr and Ca contents were at a high level, with mean values of 24.35 mg/kg and 16.86 g/kg, respectively, and Ba content (6.67 mg/kg) was very low. The Sr/Ba ratio was high, with a mean value of 4.20. At 10.55–3.90 m (section II, 351 BCE to 453 CE), the contents of Sr and Ca and Sr/Ba ratio decreased remarkably with mean values of 6.13 mg/kg, 3.27 g/kg, and 0.26, respectively, and Ba showed an increasing trend from the bottom upward but fluctuated markedly. Above 3.90 m (section III, after 453 CE), the contents of Sr and Ca and Sr/Ba ratio maintained low values, and Ba increased obviously to an average of 76.40 mg/kg.

5. Discussion

5.1. Changes in the Hydrological Environment Recorded in Profile T1312S and Core ZK04

Profile T1312S and core ZK04 are located in the coastal lowlands on the north and south banks of Hangzhou Bay and are sensitive to changes in the hydrological environment related to the climate and sea-level fluctuations. The local water level and salinity can be inferred from the organic carbon content and composition and the distribution of alkaline earth metals [43,54,55]. The hydrological environment changes recorded in profile T1312S and core ZK04 are analyzed separately below.

In profile T1312S, the low TOC contents and C/N ratios in stage I (prior to 370 BCE), as well as the noticeably enriched $\delta^{13}C$ values (Figure 5), indicate strong bacterial degradation or a source of organic matter primarily coming from marine algae [56,57]. Meanwhile, the low values of Sr and Ca indicate a non-marine environment [42,43], thereby implying that the low TOC contents and enriched $\delta^{13}C$ values resulted from bacterial degradation. However, the low levels of Ba suggest that the environment is affected by low-salinity water [43,58]. The above inference aligns with lithological characteristics, including rust spots and traces of oxidized plant roots, indicating that this section of the profile was situated in an area with a low water level and weak soil formation, which is more plausibly described as a supratidal environment. During stage II (370 BCE to 120 CE), there were increased contributions from terrestrial C_3 plants resulting in higher C/N ratios and lower $\delta^{13}C$ values [59,60]. Archaeological excavations also indicate that this layer of Yue cultural deposits during the Warring States Period may have been the result of anthropogenic activities. The low levels of Sr, Ca, and Ba suggest that this was a tidal freshwater environment. During stage III (120–895 CE), the productivity of C_3 plants increased remarkably, as evidenced by the considerable increases in TOC and C/N ratios, and the obviously decreased $\delta^{13}C$ values. Meanwhile, the growth in the contents of Sr and Ca suggests saltwater intrusion, especially at 62–60 cm (722–838 CE). The above sedimentary records suggest the possibility of rising local water levels induced by relative sea-level rise during this period. This may have contributed to the emergence of a low-salinity marsh and the preservation of organic matters within the stratigraphy. During stage IV (since 895 CE), the oxidized plant remains in the lithology, the decline in TOC content and C/N ratio, as well as the increased $\delta^{13}C$ values and the reduction in the contents of Sr and Ca, indicate a decrease in the local water level at the Dahutou site. The environment has reverted to a subaerially exposed environment dominated by pedogenesis, and the obvious increase in Ba content denotes an upsurge in the terrestrial input, implying that the site had evolved into a fluvial plain [43].

Below 10.55 m (approximately 5900 BCE), the higher contents of Sr and Ca and the low content of Ba in sediment core ZK04 clearly reflects a seawater inundation (Figure 7). Previous studies have indicated that the core was located in the paleo-Taihu estuary during this period [61]. There was a rapid decrease in Sr and Ca contents, while Ba content increased during 351 BCE to 453 CE (10.55–3.90 m), indicating that the core site evolved into a fluvial environment. Fluctuations in Ba content indicate that the core site was affected by low-salinity water intrusion induced mainly by the flood currents of tides [42,43]. In particular, the content of Ba consistently exhibited low values from 32 CE to 488 CE, reflecting the frequent low-salinity water intrusion during this period. In addition, the large number of yellowish mud intraclasts at 5.22–5.77 m (23 BCE to 15 CE) may indicate flooding events of the East Tiaoxi River [54]. After 488 CE, the notable increase in the Ba content indicates an enhancement in freshwater runoff and associated terrestrial supply, suggesting that the core site became a full-fledged alluvial plain of the East Tiaoxi River and was no longer affected by the salinity intrusion.

5.2. Climate Change Recorded in Profile T1718N

Changes in the proxies of chemical weathering in profile T1718N indicate fluctuations in the degree of climatic warmth and humidity in the East Tiaoxi River basin. The warm and humid climate enhances chemical weathering in the source area, leading to the loss of Na, K, and Ca with surface water and the enrichment of Al in detrital minerals [44,45].

Meanwhile, Na is more prone to lose relative to K [50]. Therefore, the high values of each chemical weathering index and the low value of Na_2O/K_2O in unit b of profile T1718N indicate a warm and humid climate during the period from 695 BCE to 1371 CE (Figure 6), which includes two previously reported warm periods, i.e., the Qin-Han (corresponding to the Roman Warm Period in Europe; 250 BCE to 400 CE) and Sui-Tang (589 to 907 CE) Warm Periods (Figure 8).

Previous studies demonstrated that the climate in Europe was warm and humid from the 1st century BCE to the middle of the 4th century CE [62,63], which was called the Roman Warm Period as it corresponded to the time of the Ancient Roman Empire [12]. Ljungqvist [64] reconstructed a mean temperature curve for the Northern Hemisphere (30–90° N) (Figure 8e) and suggested that the Northern Hemisphere was generally warm during the Roman Warm Period. In China, Zhu [11] reconstructed the temperature based on phenological records from historical documents (Figure 8f), revealing a warm period consistent with the Roman Warm Period, which he named the Qin-Han Warm Period. Later, Ge et al. [9,65,66] also reconstructed the winter temperatures in East China (Figure 8g), as well as the dry and wet climate in the Jiangnan region (Figure 8h) based on the historical documents. These findings revealed that the Qin-Han Warm Period was characterized by higher temperatures and increased humidity. Therefore, the sedimentary records in profile T1718N (Figure 8a) in this study, along with the previous research findings, supports the conclusion that the Roman or Qin-Han Warm Period was a widespread occurrence in the Northern Hemisphere.

The profile T1718N from this study further demonstrates that the East Tiaoxi River basin experienced consistent high levels of chemical weathering following the Qin-Han Warm Period until the end of the Tang Dynasty, when it declined significantly (Figure 8a). This is in agreement with the Sui-Tang Warm Period (589–907 CE) proposed by Zhu [11], who suggested that the temperature in China during this era was 1 °C higher than the average temperature in mid-1970s (Figure 8f). The reconstructed winter temperature anomaly in East China (Figure 8g) and humidity index in the Jiangnan region (Figure 8h) by Ge et al. [9,66] also support that this period was characterized by a warm and humid climate. However, the reconstructed mean temperature of Northern Hemisphere (30–90° N) in Figure 8e indicates that this period was still in the process of warming [64]. Some studies claimed that this period belonged to the Dark Ages Cold Period after the end of the Roman Warm Period [12,67]. The $\delta^{18}O$ record of the Dunde Ice Core from inland Asia also suggests that the western part of China was cold at this time [68]. Thus, it is suggested that the Sui-Tang Warm Period was potentially a regional climatic event that happened in central and eastern China.

5.3. Response of Hydraulic Engineering to Changes in Climate and Hydrological Environment

Figure 8 compares the major hydraulic engineering with the climatic and hydrological environmental change on the coast of Hangzhou Bay from the East Zhou dynasty. There are major events of seawall construction to prevent tidal surge and salinity intrusion at 493–473 BCE (Eastern Zhou dynasty), 50 CE (Han dynasty), 630 CE (Tang dynasty), 686 CE (Tang dynasty), 722 CE (Tang dynasty), and 910 CE (Wuyue State following the collapse of Tang dynasty). Additionally, the river flooding control projects comprise the enclosure of Jianhu Lake in the south coast of Hangzhou Bay at 140 CE and the South Lake and Great Xixian Levee of the East Tiaoxi River basin in the north coast of Hangzhou Bay at 173 CE during the Eastern Han dynasty. Figure 8 indicates that the above events of hydraulic engineering are consistent with the warm climate and salinity intrusion on both coasts of Hangzhou Bay.

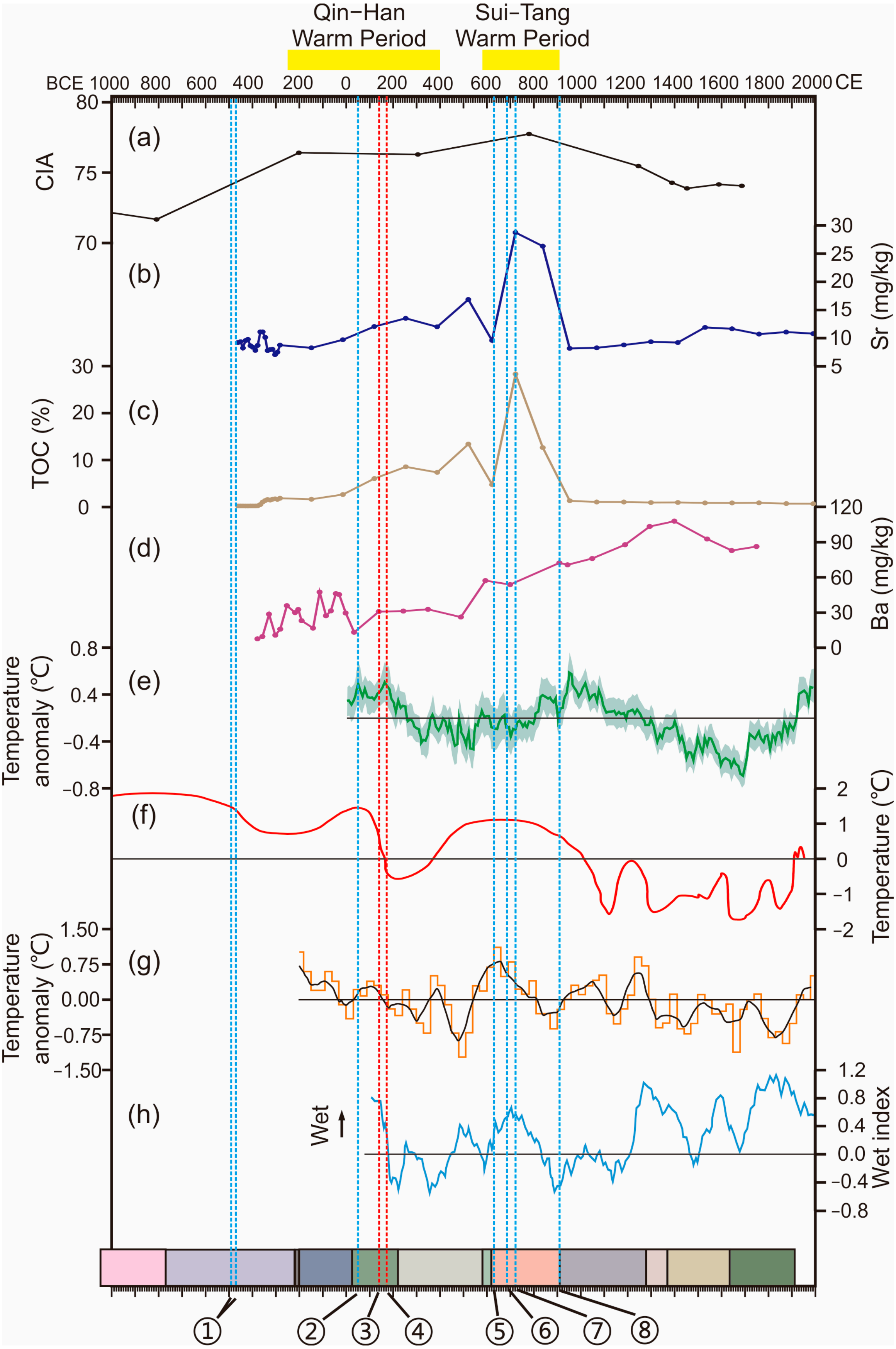

Figure 8. Comparison of the sedimentary stratigraphic records of climate change and hydrological events in this study (**a**–**d**) with the results of previous studies (**e**–**h**) over the past 3000 years: (**a**) CIA

of profile T1718N at the Tiaotou site; (**b**) Change in Sr content of profile T1312S at the Dahutou site, reflecting the degree of saltwater influence; (**c**) Change in TOC content of profile T1312S, reflecting the preservation of organic matter related to the local water level; (**d**) Ba elemental changes in core ZK04, reflecting freshwater discharge and the low-salinity water intrusion; (**e**) Reconstructed mean temperature based on 30 records in the Northern Hemisphere (90–30° N) compared to the mean instrumental temperature during 1961–1990, along with double standard deviation error bars [64]; (**f**) Temperature change in China according to historical documents [11]; (**g**) Winter temperature anomaly (resolution of 10–30 years) for the past 2000 years in East China [9,66]; (**h**) A 100-year moving average of the humidity index in the Jiangnan region sourced from historical documents [66]. The yellow bars at the top represent the two warm periods. The blue vertical dashed lines represent the seawall projects and the red vertical dashed lines are river levees and the enclosure of lakes in the historical period. Explanation of ①–⑧ is same as in Figure 2. The colored bar of dynasties in China same as in Figure 2 is also indicated at the bottom.

The construction of seawalls at 493–473 BCE by the State of Yue falls outside the recorded years of profile T1312S and core ZK04, and the resolution of profile T1718N is inadequate to determine the climatic environment of the study area during this time (Figure 8a–d). However, the temperature reconstructed by Zhu [11] indicates that this was a warm period. Sedimentary records of both cores from Chen et al. [61] in the Taihu Plain indicate a rise in local water levels and associated lake expansions around 2800 years ago, suggesting a warmer climate or a rise in relative sea level. A previous study suggested more extreme storms in Hangzhou Bay under the background of a warmer climate [69]. Consequently, it is plausible that the construction of seawalls by the Yue State was a reaction to the frequent storm tides.

The construction of seawalls in 50 CE and management projects of river flood at 140 CE and 173 CE coincide with the Qin-Han Warm Period. The cultural layer accumulation was interrupted around 120 CE in profile T1312S on the southern coast of Hangzhou Bay. This disruption was accompanied by a noticeable rise in Sr and TOC contents, which implies a transition to a low-salinity marsh environment (Figures 5 and 8b,c). The consistently low Ba contents in core ZK04 on the north coast (Figure 8d) between 32 CE and 488 CE suggest frequent occurrences of salinity intrusion during this phase. It is, thus, speculated that climate warming caused the relative sea level in Hangzhou Bay to rise, resulting in elevated local water levels and salinity intrusion on both the north and south coasts of the bay. Therefore, in 50 CE, a seawall in Qiantang (Figure 1c) was constructed [51] in response to saltwater intrusion. Literature records indicate frequent flooding events in the East Tiaoxi River basin during the Han Dynasty prior to 172 CE [26,27]. The deposition of approximately 0.55 m thick mud intraclasts at about 23 BCE to 15 CE (Figure 7) in core ZK04 may indicate the frequent flooding events in the East Tiaoxi River basin. Li et al. [36] also detected flood deposits dating back to 85 CE in the buried channel at the Tiaotou site, indicating that extreme precipitation events became more frequent during the Qin-Han Warm Period in the study area. It is suggested that these events were the direct cause of the projects including the enclosure of Jianhu Lake in 140 CE and South Lake in 173 CE, and the construction of the Great Xixian Levee in 173 CE for river flood management.

In the 7th and early 8th centuries CE, the Tang government constructed large-scale seawalls on the south and north coasts of Hangzhou Bay (Figure 1c), corresponding to the climatic and hydrological conditions of the Sui-Tang Warm Period (Figure 8). In 910 CE (just after the collapse of Tang dynasty), the Wuyue State constructed seawalls in Qiantang on a larger scale than the seawalls of Han Dynasty (Figure 1c). During this warm period, the Sr contents in profile T1312S at the Dahutou site were remarkably higher than that of the salinity intrusion event witnessed during the Qin-Han Warm Period. This indicates the possibility of a more intensified or frequent saltwater intrusion, which could explain the construction of the larger-scale seawalls mentioned above. In contrast, the obvious increase in Ba content from the Sui-Tang Warm Period in core ZK04 (Figure 8d) indicates a greater supply of terrestrial sediments [42,43]. There may be several reasons why a salinity intrusion signal is absent at that time in ZK04. Firstly, before the Tang Dynasty, there was already effective management of the hydrological environment against salinity intrusion in the upper part of the north coast of Hangzhou Bay. During the Tang Dynasty, the seawalls were mainly constructed in east part of the north coast (Yanguan Seawall, Figure 1c), and it was not until the Wuyue State that seawalls were built again at Qiantang on the head of bay, which also indicates less risk of salinity intrusion for most of the Tang Dynasty. Secondly, according to Wu [27], the construction of the Great Xixian Levee in the Han Dynasty diverted the East Tiaoxi River to flow northward through the northwest of Liangzhu City before discharging into Taihu Lake (Figure 1b,c). Thus, the remarkable increase in the Ba content at core ZK04 from Sui-Tang Warm Period may also indicate that the warmer climate increased the freshwater discharge from East Tiaoxi River, thus preventing the salinity intrusion. A third speculation is that the Great Xixian Levee was continuously built after its initiation at 173 CE, which led to the increased freshwater discharge of East Tiaoxi River into Taihu Lake by the Tang dynasty as, according to the historical documents, the construction of the Levee remained incomplete until the Song dynasty [27].

The coordination of the three hydraulic engineering phases with a warmer climate, increased precipitation, enhanced saltwater intrusion, and rising local water levels implies that warmer climate periods in the Hangzhou Bay coastal regions are typically accompanied by elevated relative sea levels and intensified storm events. The funnel shape of Hangzhou Bay may further amplify the magnitude of relative sea-level rise, especially the storm surges during the typhoon events [34,70,71]. Therefore, seawalls were constructed in the region to cope with marine hazards. However, over the past 1000 years or so, salinity intrusion was no longer recorded in the sediments of T1312S and ZK04, which may indicate that human societies have better managed seawalls and salinity intrusion.

6. Conclusions

In this study, we collected profile T1312S from the Dahutou site on the southern coast of Hangzhou Bay, profile T1718N from the Tiaotou site on the northern coast of Hangzhou Bay, and sediment core ZK04 in the middle reaches of East Tiaoxi River. By applying multi-proxy analyses including chronology, sedimentology, and geochemistry, we examined the climate and hydrological events in the coastal area of Hangzhou Bay over the past 3000 years. Additionally, we compared human society's hydraulic engineering with the changes in the climatic and hydrological environments and reached the following main conclusions.

(1) Geochemical analyses of the profile T1718N indicate strong chemical weathering in East China from 695 BCE to 1371 CE, particularly at ca. 200 BCE–900 CE, revealing warm and humid climatic conditions during a phase that encompasses two warm periods, the Qin-Han Warm Period and the Sui-Tang Warm Period.

(2) Alkaline earth metals in profile T1312S and core ZK04 demonstrate that salinity intrusion occurred frequently on the north and south coasts of Hangzhou Bay during the Qin-Han Warm Period, as well as the Sui-Tang Warm Period. The formation of low-salinity marsh at the Dahutou site from approximately 120 CE to 895 CE indicates a simultaneous rise in the local water level and intensification of saltwater intrusion, suggesting a relative sea-level rise in the region during the Qin-Han and Sui-Tang Warm Periods. The above relative sea-level rise and frequent salinity intrusion explains the construction of seawalls in the Eastern Han and Tang Dynasties.

(3) Sediments in the East Tiaoxi River basin on the north coast of Hangzhou Bay also record flooding events about 2000 years ago, reflecting the frequency of heavy precipitation events in the study area during the Qin-Han Warm Period, which explains the river flood management projects on the north and south coasts of Hangzhou Bay during this period.

Author Contributions: Conceptualization, Z.W.; Methodology, X.L., W.Z. and Z.W.; Formal analysis, Z.W.; Investigation, X.L., X.Y., S.L., W.Z., Z.C. and Z.W.; Data curation, X.L.; Writing—original draft, X.L. and Z.W.; Writing—review & editing, X.Y. and S.L.; Project administration, Z.W.; Funding acquisition, Z.W. All authors have read and agreed to the published version of the manuscript.

Funding: This research was funded by Key R&D Program of Zhejiang Province, China (grant No. 2022C03141).

Institutional Review Board Statement: Not applicable.

Informed Consent Statement: Not applicable.

Data Availability Statement: Data is contained within this article.

Acknowledgments: Authors are grateful to two reviewers for their valuable comments.

Conflicts of Interest: The authors declare no conflicts of interest.

References

1. Caballero, M.; Ortega, B.; Valadez, F.; Metcalfe, S.; Macias, J.L.; Sugiura, Y. Sta. Cruz Atizapán: A 22-ka lake level record and climatic implications for the late Holocene human occupation in the Upper Lerma Basin, Central Mexico. *Palaeogeogr. Palaeoclim. Palaeoecol.* **2002**, *186*, 217–235. [CrossRef]
2. Wanner, H.; Beer, J.; Bütikofer, J.; Crowley, T.J.; Cubasch, U.; Flückiger, J.; Goosse, H.; Grosjean, M.; Joos, F.; Kaplan, J.O.; et al. Mid- to Late Holocene climate change: An overview. *Quat. Sci. Rev.* **2008**, *27*, 1791–1828. [CrossRef]
3. Wang, T.; Surge, D.; Mithen, S. Seasonal temperature variability of the Neoglacial (3300–2500BP) and Roman Warm Period (2500–1600BP) reconstructed from oxygen isotope ratios of limpet shells (Patella vulgata), Northwest Scotland. *Palaeogeogr. Palaeoclim. Palaeoecol.* **2012**, *317–318*, 104–113. [CrossRef]
4. Biagetti, S.; Merlo, S.; Adam, E.; Lobo, A.; Conesa, F.C.; Knight, J.; Bekrani, H.; Crema, E.R.; Alcaina-Mateos, J.; Madella, M. High and Medium Resolution Satellite Imagery to Evaluate Late Holocene Human–Environment Interactions in Arid Lands: A Case Study from the Central Sahara. *Remote. Sens.* **2017**, *9*, 351. [CrossRef]
5. Thompson, L.G. Ice core evidence for climate change in the Tropics: Implications for our future. *Quat. Sci. Rev.* **2000**, *19*, 19–35. [CrossRef]
6. Hu, C.; Henderson, G.M.; Huang, J.; Xie, S.; Sun, Y.; Johnson, K.R. Quantification of Holocene Asian monsoon rainfall from spatially separated cave records. *Earth Planet. Sci. Lett.* **2008**, *266*, 221–232. [CrossRef]
7. Ols, C.; Girardin, M.P.; Hofgaard, A.; Bergeron, Y.; Drobyshev, I. Monitoring Climate Sensitivity Shifts in Tree-Rings of Eastern Boreal North America Using Model-Data Comparison: Shifts in Tree Growth Sensivity to Climate. *Ecosystems* **2017**, *21*, 1042–1057. [CrossRef]
8. Qiang, M.; Jin, Y.; Liu, X.; Song, L.; Li, H.; Li, F.; Chen, F. Late Pleistocene and Holocene aeolian sedimentation in Gonghe Basin, northeastern Qinghai-Tibetan Plateau: Variability, processes, and climatic implications. *Quat. Sci. Rev.* **2016**, *132*, 57–73. [CrossRef]
9. Ge, Q.; Zheng, J.; Fang, X.; Man, Z.; Zhang, X.; Zhang, P.; Wang, W.-C. Winter half-year temperature reconstruction for the middle and lower reaches of the Yellow River and Yangtze River, China, during the past 2000 years. *Holocene* **2003**, *13*, 933–940. [CrossRef]
10. Zheng, J.; Wang, W.-C.; Ge, Q.; Man, Z.; Zhang, P. Precipitation variability and extreme events in Eastern China during the past 1500 years. *Terr. Atmospheric Ocean. Sci.* **2006**, *17*, 579–592. [CrossRef]
11. Zhu, K. A preliminary study of climate change in China over the past 5000 years. *Acta Archaeol. Sinica.* **1972**, *1*, 15–38. (In Chinese)
12. Lamb, H.H. *Climate: Present, Past and Future. Volume 2: Climatic History and the Future*; Routledge: London, UK, 1977; p. 837.
13. Bond, G.; Showers, W.; Cheseby, M.; Lotti, R.; Almasi, P.; Demenocal, P.; Priore, P.; Cullen, H.; Hajdas, I.; Bonani, G. A Pervasive Millennial-Scale Cycle in North Atlantic Holocene and Glacial Climates. *Science* **1997**, *278*, 1257–1266. [CrossRef]
14. Yamada, K.; Kamite, M.; Saito-Kato, M.; Okuno, M.; Shinozuka, Y.; Yasuda, Y. Late Holocene monsoonal-climate change inferred from Lakes Ni-no-Megata and San-no-Megata, northeastern Japan. *Quat. Int.* **2010**, *220*, 122–132. [CrossRef]
15. Ge, Q.; Liu, J.; Fang, X.; Yang, B.; Hao, Z.; Shao, X.; Zheng, J. General characteristics of temperature change and centennial warm periods during the past 2000 years. *Acta Geogr. Sin.* **2013**, *68*, 579–592. (In Chinese)
16. Shao, S.; Wu, D.; Wang, T.; Yuan, Z.; Li, Y.; Feng, X.; Zhou, A. Late Holocene hydrological variations recorded by sediments from Lake Gongka in the Hengduan Mountains and their linkage with the India summer monsoon. *J. Lake Sci.* **2023**, *35*, 1126–1138. (In Chinese)
17. Currás, A.; Zamora, L.; Reed, J.; García-Soto, E.; Ferrero, S.; Armengol, X.; Mezquita-Joanes, F.; Marqués, M.; Riera, S.; Julià, R. Climate change and human impact in central Spain during Roman times: High-resolution multi-proxy analysis of a tufa lake record (Somolinos, 1280 m asl). *CATENA* **2012**, *89*, 31–53. [CrossRef]
18. Silva-Sánchez, N.; Cortizas, A.M.; Abel-Schaad, D.; López-Sáez, J.; Mighall, T. Influence of climate change and human activities on the organic and inorganic composition of peat during the 'Little Ice Age' (El Payo mire, W Spain). *Holocene* **2016**, *26*, 1290–1303. [CrossRef]
19. Yao, H. *Outline of Chinese Water Conservancy History*; China Water and Power Press: Beijing, China, 1987; p. 599. (In Chinese)
20. Chen, J. *Seawalls–Coastal Changes and Seawall Engineering in China*; People's Publishing House: Beijing, China, 2000; p. 161. (In Chinese)
21. Shang, Y.; Park, H.-D.; Yang, Z.; Chen, S.; Lin, D. Deposition rate and interaction of human-riverine from height increase and permanent function of an 1180 years weir in Southeast China. *Sci. China Earth Sci.* **2014**, *57*, 323–336. [CrossRef]

22. Dalton, M.; Spencer, N.; Macklin, M.G.; Woodward, J.C.; Ryan, P. Three thousand years of river channel engineering in the Nile Valley. *Geoarchaeology* **2023**, *38*, 565–587. [CrossRef]
23. Liu, B.; Wang, N.; Chen, M.; Zhuang, Y. Earliest hydraulic enterprise in China 5100 years ago. *Proc. Natl. Acad. Sci. USA* **2017**, *114*, 13637–13642. [CrossRef]
24. Wang, J. *The Jianhu Lake System and the Civilization of Yue*; People's Publishing House: Beijing, China, 2008; p. 288. (In Chinese)
25. Qiu, Z.; Chen, P. *History of the Eastern Zhejiang Canal*; Chinese Literature and History Press: Beijing, China, 2014; p. 491. (In Chinese)
26. Zhao, Y. *Cultures of the South Lake at Yuhang*; Oriental Museum: Chicago, IL, USA, 2007; pp. 20–29. (In Chinese)
27. Wu, W. Several geographical changes in Hangzhou. *Hist. Geogr.* **1987**, *1*, 176–184. (In Chinese)
28. Zhejiang Provincial Institute of Cultural Relics and Archaeology. *A Comprehensive Study of Liangzhu Ancient City*; Cultural Relics Press: Beijing, China, 2019; p. 482. (In Chinese)
29. Wang, G.; Zhou, C.; Zhang, Z. Main hydrological characteristics of the tidal zone of the Qiantang River. *Hydrology* **1982**, *04*, 55–57. (In Chinese)
30. Shangyu County Records Compilation Committee. *Shangyu County Records*; Zhejiang People's Publishing House: Hangzhou, China, 1990; p. 875. (In Chinese)
31. Qian, N.; Xie, H.; Zhou, Z.; Li, G. Recent processes in the mouth shoal of the Qiantang River estuary. *Acta Geogr. Sin.* **1964**, *30*, 124–142. (In Chinese)
32. Chen, J.; Luo, Z.; Chen, D.; Xu, H.; Qiao, P. Formation of mouth shoal and its historical evolution in the estuary of the Qiantang River. *Acta Geogr. Sin.* **1964**, *30*, 109–123. (In Chinese)
33. Xie, Y. *The Effects of Regulation and Reclamation in Qiantang Estuary on Storm Surge at Hangzhou Bay*; Ocean University of China: Qingdao, China, 2006. (In Chinese)
34. Wang, S.; Ge, J.; Kilbourne, K.H.; Wang, Z. Numerical simulation of mid-Holocene tidal regime and storm-tide inundation in the south Yangtze coastal plain, East China. *Mar. Geol.* **2020**, *423*, 106134. [CrossRef]
35. He, Z.; Yu, Z.; Shi, H.; Li, Z.; Li, L. Study on the impact mechanism of Typhoon Canhong on the hydrodynamic characteristics of Hangzhou Bay. In *Ocean Engineering Society. Proceedings of the Twentieth China Ocean (Shore) Engineering Symposium (II)*; Hohai University Press: Nanjing, China, 2022; pp. 397–402. (In Chinese)
36. Li, X.; Lin, S.; Wang, Z. The sedimentary stratigraphic records of copper casting activities during the Late Shang—Early Western Zhou periods at the Tiaotou site in Yuhang, Zhejiang Province. *Quat. Sci.* **2024**, *44*, 128–143.
37. Reimer, P.J.; Austin, W.E.N.; Bard, E.; Bayliss, A.; Blackwell, P.G.; Ramsey, C.B.; Butzin, M.; Cheng, H.; Edwards, R.L.; Friedrich, M.; et al. The IntCal 20 Northern Hemisphere radiocarbon age calibration curve (0–55 cal kBP). *Radiocarbon* **2020**, *62*, 725–757. [CrossRef]
38. Durcan, J.A.; King, G.E.; Duller, G.A. DRAC: Dose rate and age calculator for trapped charge dating. *Quat. Geochronol.* **2015**, *28*, 54–61. [CrossRef]
39. Galbraith, R.; Roberts, R. Statistical aspects of equivalent dose and error calculation and display in OSL dating: An overview and some recommendations. *Quat. Geochronol.* **2012**, *11*, 1–27. [CrossRef]
40. Murray, A.; Wintle, A. Luminescence dating of quartz using an improved single-aliquot regenerative-dose protocol. *Radiat. Meas.* **2000**, *32*, 57–73. [CrossRef]
41. Cui, M.; Wang, Z.; Rao, K.N.; Sangode, S.J.; Saito, Y.; Chen, T.; Kulkarni, Y.R.; Kumar, K.C.V.N.; Demudu, G. A mid- to late-Holocene record of vegetation decline and erosion triggered by monsoon weakening and human adaptations in the south-east Indian Peninsula. *Holocene* **2017**, *27*, 1976–1987. [CrossRef]
42. Wang, A.; Wang, Z.; Liu, J.; Xu, N.; Li, H. The Sr/Ba ratio response to salinity in clastic sediments of the Yangtze River Delta. *Chem. Geol.* **2021**, *559*, 119923. [CrossRef]
43. Huang, J.; Lei, S.; Tang, L.; Wang, A.; Wang, Z. Mid-Holocene environmental change and human response at the Neolithic Wuguishan site in the Ningbo coastal lowland of East China. *Holocene* **2020**, *30*, 1591–1605. [CrossRef]
44. Nesbitt, H.; Young, G. Prediction of some weathering trends of plutonic and volcanic rocks based on thermodynamic and kinetic considerations. *Geochim. Et Cosmochim. Acta* **1984**, *48*, 1523–1534. [CrossRef]
45. Nesbitt, H.W.; Young, G.M. Formation and diagenesis of weathering profiles. *J. Geol.* **1989**, *97*, 129–147. [CrossRef]
46. Harnois, L. The CIW index: A new chemical index of weathering. *Sediment. Geol.* **1988**, *55*, 319–322. [CrossRef]
47. Fedo, C.M.; Nesbitt, H.W.; Young, G.M. Unravelling the effects of potassium metasomatism in sedimentary rocks and paleosols, with implications for paleoweathering conditions and provenance. *Geology* **1995**, *23*, 921–924. [CrossRef]
48. McLennan, S.M. Weathering and Global Denudation. *J. Geol.* **1993**, *101*, 295–303. [CrossRef]
49. Feng, L.; Chu, X.; Zhang, Q.; Zhang, T. CIA (Chemical Index of Alteration) and its applications in the Neoproterozoic clastic rocks. *Earth Sci. Front.* **2003**, *10*, 539–544. (In Chinese)
50. Nesbitt, H.; Markovics, G.; Price, R. Chemical Processes affecting alkalis and alkaline earths during continental weathering. *Geochim. Et Cosmochim. Acta* **1980**, *44*, 1659–1666. [CrossRef]
51. Wang, G. *Literature Integration about Qiantang River, Hangzhou Manual (Volume II: Historical Materials of Qiantang River Seawalls II)*; Hangzhou Publishing House: Hangzhou, China, 2014; p. 133. (In Chinese)
52. Chen, Q. The ancient Lake Jianhu with spatial regard to its role in the agriculture of the Shanhui Plain. *Acta Geogr. Sin.* **1962**, *28*, 187–202. (In Chinese)

53. Blaauw, M. Methods and code for 'classical' age-modelling of radiocarbon sequences. *Quat. Geochronol.* **2010**, *5*, 512–518. [CrossRef]
54. Huang, J.; Li, Y.; Ding, F.; Zheng, T.; Meadows, M.E.; Wang, Z. Sedimentary records of mid-Holocene coastal flooding at a Neolithic site on the southeast plain of Hangzhou Bay, east China. *Mar. Geol.* **2021**, *431*, 106380. [CrossRef]
55. Zhang, W.; Zheng, T.; Wang, Z.; Meadows, M.E. Reconstruction of coastal flooding processes and human response at the end of the Liangzhu Culture, East China. *Quat. Sci. Rev.* **2022**, *293*, 107705. [CrossRef]
56. Meyers, P.A. Preservation of elemental and isotopic source identification of sedimentary organic matter. *Chem. Geol.* **1994**, *114*, 289–302. [CrossRef]
57. Lamb, A.L.; Wilson, G.P.; Leng, M.J. A review of coastal palaeoclimate and relative sea-level reconstructions using δ13C and C/N ratios in organic material. *Earth-Sci. Rev.* **2006**, *75*, 29–57. [CrossRef]
58. Coffey, M.; Dehairs, F.; Collette, O.; Luther, G.; Church, T.; Jickells, T. The behaviour of dissolved barium in estuaries. *Estuarine Coast. Shelf Sci.* **1997**, *45*, 113–121. [CrossRef]
59. Meyers, P.A. Organic geochemical proxies of paleoceanographic, paleolimnologic, and paleoclimatic processes. *Org. Geochem.* **1997**, *27*, 213–250. [CrossRef]
60. Wilson, G.P.; Lamb, A.L.; Leng, M.J.; Gonzalez, S.; Huddart, D. Variability of organic δ13C and C/N in the Mersey Estuary, U.K. and its implications for sea-level reconstruction studies. *Estuar. Coast. Shelf Sci.* **2005**, *64*, 685–698. [CrossRef]
61. Chen, T.; Ryves, D.B.; Wang, Z.; Lewis, J.P.; Yu, X. Mid- to late Holocene morphological and hydrological changes in the south Taihu area of the Yangtze delta plain, China. *Palaeogeogr. Palaeoclimatol. Palaeoecol.* **2018**, *498*, 127–142. [CrossRef]
62. Moberg, A.; Sonechkin, D.M.; Holmgren, K.; Datsenko, N.M.; Karlén, W. Highly variable Northern Hemisphere temperatures reconstructed from low- and high-resolution proxy data. *Nature* **2005**, *433*, 613–617. [CrossRef]
63. Büntgen, U.; Tegel, W.; Nicolussi, K.; McCormick, M.; Frank, D.; Trouet, V.; Kaplan, J.o.; Herzig, F.; Heussner, K.-U.; Wanner, H.; et al. 2500 years of European climate variability and human susceptibility. *Science* **2011**, *331*, 578–582. [CrossRef]
64. Ljungqvist, F.C. A new reconstruction of temperature variability in the extra-tropical northern hemisphere during the last two millennia. *Geogr. Ann. Ser. A Phys. Geogr.* **2010**, *92*, 339–351. [CrossRef]
65. Ge, Q.; Zheng, J.; Fang, X.; Man, Z.; Zhang, X.; Zhang, P.; Wang, W. Temperature changes of winter-half-year in Eastern China during the past 2000 years. *Quat. Sci.* **2002**, *22*, 166–173. (In Chinese)
66. Ge, Q.; Zheng, J.; Hao, Z.; Liu, H. General characteristics of climate changes during the past 2000 years in China. *Sci. China Earth Sci.* **2012**, *42*, 934–942. [CrossRef]
67. Wang, S. Dark Ages Cold Period. *Adv. Clim. Change Res.* **2011**, *7*, 233–234. (In Chinese)
68. Yao, T.; Thompson, L. Trends and features of climatic changes in the past 5000 years recorded by the Dunde ice core. *Ann. Glaciol.* **1992**, *16*, 21–24.
69. Wu, Y.; Huang, X.; Zheng, X.; Meadows, M.E.; Wang, Z. Sedimentary records of mid-Holocene extreme storm events on the north bank of Hangzhou Bay, East China. *Mar. Geol.* **2022**, *451*, 106891. [CrossRef]
70. Talke, S.A.; Orton, P.; Jay, D.A. Increasing storm tides in New York Harbor, 1844-2013. *Geophys. Res. Lett.* **2014**, *41*, 3149–3155. [CrossRef]
71. Wang, S.; Ge, J.; Meadows, M.E.; Wang, Z. Reconstructing a late Neolithic extreme storm event on the southern Yangtze coast, East China, based on sedimentary records and numerical modeling. *Mar. Geol.* **2022**, *443*, 106687. [CrossRef]